Industrial Chemistry & Materials

PAPER
Zi-Rong Tang, Yi-Jun Xu *et al.*
Cocatalyst-modified In$_2$S$_3$ photocatalysts for C–N coupling
of amines integrated with H$_2$ evolution

ROYAL SOCIETY
OF **CHEMISTRY**

CM
Industrial Chemistry & Materials

ROYAL SOCIETY OF CHEMISTRY

PAPER

Check for updates

Cocatalyst-modified In₂S₃ photocatalysts for C–N coupling of amines integrated with H₂ evolution†

Yu Chen, Chang-Long Tan, Jing-Yu Li, Ming-Yu Qi, Zi-Rong Tang [ID]* and Yi-Jun Xu [ID]*

Photocatalytic hydrogen (H₂) production coupled with selective oxidation of organic compounds into high-value-added organic intermediates has expansive prospects in the utilization and transformation of solar energy, which meets the development requirements of green chemistry. In this work, high-efficiency hole cocatalyst PdS-decorated In₂S₃ flower-like microspheres are fabricated for the effective visible-light-driven C–N coupling of amines to imines coupled with H₂ evolution. Owing to the establishment of the internal electric field, which further boosts the transfer of photoexcited holes to PdS, PdS–In₂S₃ exhibits distinctly enhanced photocatalytic redox performance, which is 39.8 times higher for H₂ and 14.3 times higher for *N*-benzylidenebenzylamine than that of the blank In₂S₃, along with high selectivity and stability. Furthermore, the practicability of dehydrogenation coupling of various aromatic amines to the corresponding C–N coupling products on PdS–In₂S₃ has been demonstrated and a plausible reaction mechanism has been proposed. This work is anticipated to stimulate further interest in establishing an innovative photoredox platform for selective organic synthesis coupled with H₂ evolution in a green and sustainable way.

1 Introduction

Combining photocatalytic hydrogen (H₂) production with organic transformation to generate appreciating compounds in a sustainable and green way, which eschews the consumption of non-renewable fossil fuels and extreme or high-energy-consuming reaction conditions, has garnered considerable attention in environmentally friendly and economically sustainable industrial production.[1] Imines, as one of the most important intermediates for the synthesis of pesticides, pharmaceuticals, and biologically active molecules, have inspired ongoing efforts from both academic and industrial scientists.[2,3] However, acidic (or alkaline) and high-temperature reaction conditions are usually needed to drive and catalyze the traditional imine synthesis reaction, with these reactions suffering from unsatisfactory yields and product selectivity.[4–6] Recently, the photocatalytic oxidative dehydrogenation coupling of amines in a pure oxygen (O₂) atmosphere was reported, which possesses milder and more economical conditions than conventional synthesis methods.

However, it first requires the formation of superoxide radicals by electron attack on O₂ molecules to carry out amine oxidation, which not only loses the energy of the photogenerated electrons, but also exacerbates the uncertainty of the reaction, such as through excessive oxidation and side reactions, thereby reducing the selectivity of the reaction.[7–11] In contrast, the coproduction of H₂ and value-added imines in one photoredox cycle under anaerobic conditions is a prospective scheme to fully utilize the electrons and holes generated by light for cooperative reactions to simultaneously produce valuable organic chemicals and clean fuel.[12]

Indium sulfide (In₂S₃), as a typical III–VI group metal sulfide[13–16] with an excellent visible light response,[17] low toxicity,[18] stable chemistry,[19] and a suitable band edge position,[20] has been used as photocatalyst for contaminant degradation,[21] CO₂ reduction,[22] organic coupling,[23,24] and H₂ evolution.[25] However, the photocatalytic redox efficiency of blank In₂S₃ is severely hindered by the absence of catalytically active sites and the rapid recombination of photogenerated charge carriers.[26,27] PdS has been proven as an oxidation cocatalyst with excellent hole-trapping ability, which can effectively capture and retain holes from other photoexcited semiconductors.[28–32] Therefore, the modification of PdS as a cocatalyst onto In₂S₃ for judiciously constructing PdS–In₂S₃ composites could be an appealing strategy.[33–35] Such strategy

College of Chemistry, State Key Laboratory of Photocatalysis on Energy and Environment, Fuzhou University, Fuzhou, 350116, China.
E-mail: zrtang@fzu.edu.cn, yjxu@fzu.edu.cn

© 2024 The Author(s). Co-published by the Institute of Process Engineering, Chinese Academy of Sciences and the Royal Society of Chemistry

Ind. Chem. Mater., 2024, **2**, 289–299 | 289

could not only effectively reduce the recombination of photoexcited carriers for maximizing the utilization of photogenerated electron–hole pairs, but also change the activation energy of the interfacial photoredox reaction,[36] further enhancing the photocatalytic performance of the catalyst.

Herein, we successfully constructed a PdS–In$_2$S$_3$ binary photocatalyst through a combination of solvothermal treatment and *in situ* chemical deposition for the dual-functional photocatalytic redox reaction of dehydrocoupling of amines to imines and H$_2$. The conversion of benzylamine (BA) reached more than 95.5% over the optimal PdS–In$_2$S$_3$ photocatalyst after 4 h of reaction, which is roughly 36.1-fold higher than that of blank In$_2$S$_3$, along with a terrific *N*-benzylidenebenzylamine (*N*-BDBA) selectivity of above 99.0%. The formation of the internal electric field provides a powerful impetus for PdS to extract holes from In$_2$S$_3$, and thus effectively reduces the photogenerated carrier recombination, which leads to more photogenerated holes and electrons for the coproduction of imines and H$_2$. In addition, such a photocatalytic system is applicable to various amines, furnishing the corresponding imines with excellent selectivity and long-term stability. Mechanism studies revealed that the carbon radical (Ph·CH)NH$_2$) plays a key role in the reaction, and a plausible reaction mechanism has been suggested accordingly. It is anticipated that this work will provide insights into the rational design of In$_2$S$_3$-based composite photocatalysts to facilitate the visible-light-driven coproduction of high-value-added chemicals and clean H$_2$ fuel.

2 Results and discussion

As shown in Fig. 1a, a series of PdS-modified In$_2$S$_3$ (PdS–In$_2$S$_3$) nanospheres with different mass ratios were successfully synthesized by the combination of the solvothermal method and the *in situ* chemical deposition method. The specific morphology information of the composites was confirmed by scanning electron microscopy (SEM) and transmission electron microscopy (TEM). Fig. 1b and S1† present the SEM images of the blank In$_2$S$_3$ nanospheres with diameters ranging from 2.3 to 7.7 μm, where several thin nanosheets can be observed at the edges. The morphology of In$_2$S$_3$ is not influenced by the deposition of PdS, which can be seen in the SEM image of PdS–In$_2$S$_3$ (Fig. 1c). From the high-resolution TEM (HRTEM) image in Fig. 1d, the obvious lattice fringes of 0.277 nm and 0.618 nm are scanned in PdS–In$_2$S$_3$, corresponding to the (400) and (111) planes of In$_2$S$_3$, respectively.[15,23,25] Meanwhile, the lattice stripes of 0.324 nm and 0.185 nm belonging to the (200) and (222) planes of PdS, respectively, are also observed in the binary samples.[30,37] Additionally, the results of aberration-corrected high-angle annular dark-field scanning TEM (HAADF-STEM), elemental mapping (Fig. 1e), and energy-dispersive X-ray (EDX) spectroscopy (Fig. S2†) analyses suggest a homogeneous distribution of Pd, S, and In in the samples, demonstrating that PdS is evenly decorated onto the In$_2$S$_3$ nanospheres. In addition, the results of inductively coupled plasma-mass emission spectroscopy (ICP-MS) analysis demonstrate that the actual content of PdS in the different samples is close to the theoretical value (Table S1†).
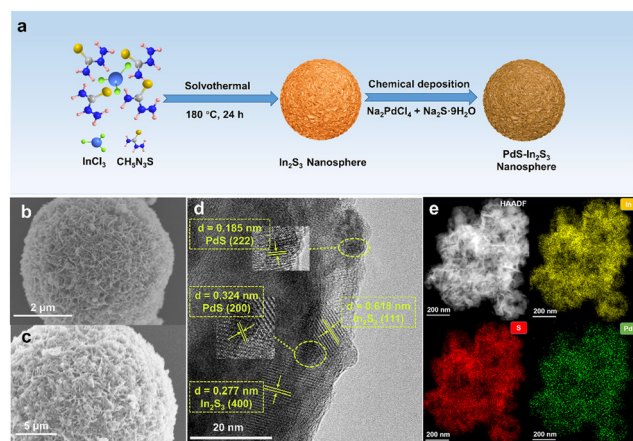

Fig. 1 (a) Schematic presentation of the synthesis of PdS–In$_2$S$_3$ samples. SEM images of (b) blank In$_2$S$_3$ and (c) 3%-PdS–In$_2$S$_3$. (d) HRTEM image of 3%-PdS–In$_2$S$_3$. (e) Element mapping results of 3%-PdS–In$_2$S$_3$.
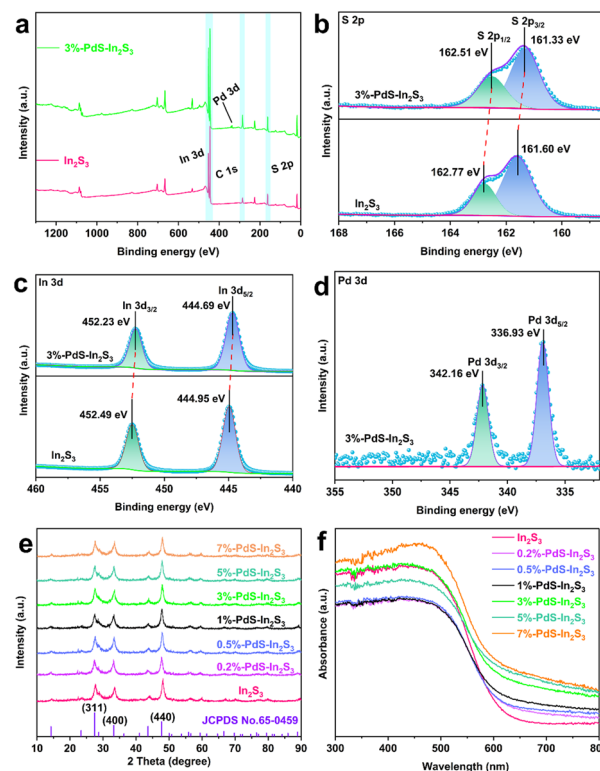

Fig. 2 (a) XPS survey spectra of blank In$_2$S$_3$ and 3%-PdS–In$_2$S$_3$. The high-resolution XPS spectra of (b) S 2p, (c) In 3d, and (d) Pd 3d of 3%-PdS–In$_2$S$_3$ and In$_2$S$_3$ composites. (e) XRD patterns and (f) DRS results for In$_2$S$_3$ and the PdS–In$_2$S$_3$ samples with varying amounts of PdS.

In order to study the valence states and element compositions of the composites, X-ray photoelectron spectroscopy (XPS) analysis was carried out. All elements (Pd, In, and S) related to In_2S_3 and PdS can be detected in the survey spectra (Fig. 2a), which are well-matched the with EDX and element mapping results. The peaks at 161.60 eV and 162.77 eV in the high-resolution S 2p XPS spectrum in Fig. 2b are categorized as S $2p_{3/2}$ and S $2p_{1/2}$, respectively, which are attributed to S^{2-}.[25] The binding energies of In 3d in Fig. 2c demonstrate that the spin–orbit doublet peaks at 444.95 eV and 452.49 eV are attributed to In $3d_{5/2}$ and In $3d_{3/2}$, respectively, which match well with In^{3+} in In_2S_3.[26] As for Pd 3d in 3%-PdS–In_2S_3, the peaks at 342.16 eV and 336.93 eV belong to the binding energies of Pd $3d_{3/2}$ and Pd $3d_{5/2}$ (Fig. 2d), which are associated with the Pd^{2+} of PdS.[37,38] Notably, with the modification of PdS, the characteristic elemental peaks associated with In_2S_3 shift toward lower binding energies, suggesting that electron migration between In_2S_3 and PdS affects the surface electron density of the photocatalysts.[39–41] X-ray diffraction (XRD) analysis was performed to characterize the properties of the crystalline phase with the different samples. The XRD patterns of the In_2S_3 and PdS–In_2S_3 containing different amounts of PdS are shown in Fig. 2e, and the main characteristic diffraction peaks of pure In_2S_3 (JCPDS no. 65-0459) at 27.4°, 33.2°, and 47.7° are detected in all materials, demonstrating that the characteristic structure of In_2S_3 is not damaged by the deposition of PdS.[18] However, the corresponding characteristic diffraction peaks of PdS are not identified in the pattern, which is due to the low load weight of PdS.[36] Furthermore, UV/vis diffuse reflectance spectroscopy (DRS) was used to measure the optical absorption properties of the different composites. As portrayed in Fig. 2f, the pristine In_2S_3 exhibits favorable visible light absorption, which is further enhanced with the increased addition of PdS. Moreover, on the basis of Tauc plots of $(\alpha h v)^2$ versus photo energy (hv),[42,43] the band gap energy (E_g) of In_2S_3 was derived to be 2.18 eV (Fig. S3†).

The photocatalytic activity of the pristine In_2S_3 and the PdS–In_2S_3 photocatalysts was measured by a dual-function
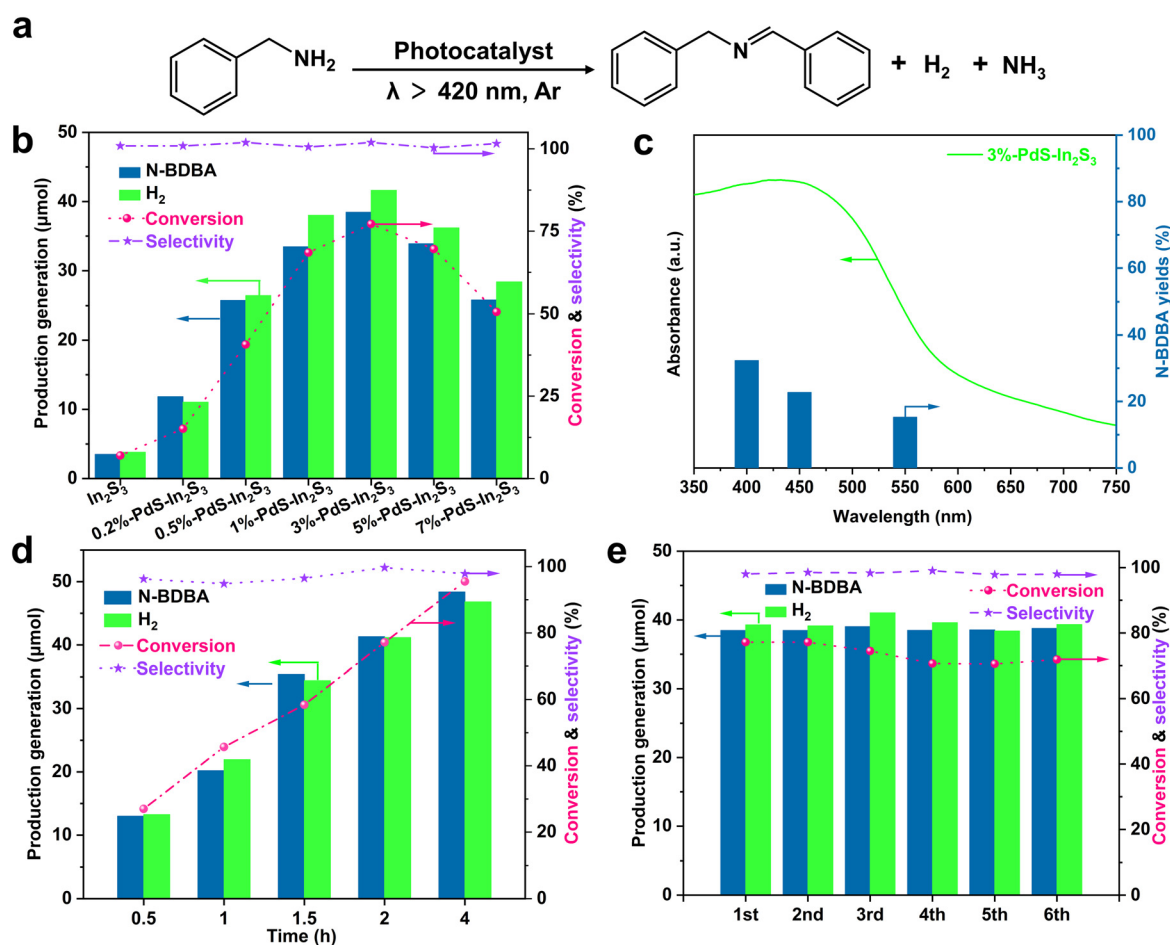

Fig. 3 (a) Schematic diagram of combined photocatalytic H_2 production and dehydrogenation coupling of BA to N-BDBA. (b) Photoredox catalyzed performance of bare In_2S_3 and x%-PdS–In_2S_3 (x = 0.2, 0.5, 1, 3, 5, and 7). (c) DRS spectrum of 3%-PdS–In_2S_3 and yields of the product over 3%-PdS–In_2S_3 under different monochromatic lights. (d) Time courses of N-BDBA and H_2 evolution over 3%-PdS–In_2S_3. (e) Photocatalytic recycling tests over 3%-PdS–In_2S_3. Reaction conditions: 5 mg of 3%-PdS–In_2S_3 photocatalyst, 0.1 mmol of BA, and 10 ml of acetonitrile (MeCN) were added to a quartz glass reactor, then the suspension was degassed under Ar for 0.5 h, and finally illuminated by visible light for 2 h.

© 2024 The Author(s). Co-published by the Institute of Process Engineering, Chinese Academy of Sciences and the Royal Society of Chemistry

Ind. Chem. Mater., 2024, **2**, 289–299 | **291**

photoredox system involving H_2 evolution and selective oxidation of BA to N-benzylidenebenzylamine (N-BDBA) (Fig. 3a). Qualitative and quantitative analyses of the liquid products were performed with the gas chromatography-mass spectrometry (GC-MS) method (Fig. S4†). As plotted in Fig. 3b, after exposure to visible light ($\lambda > 420$ nm) for 2 h, the blank In_2S_3 showed poor catalytic activity for N-BDBA generation and H_2 production (2.68 μmol and 1.05 μmol, respectively). After being modified by the cocatalyst PdS, the performance of the PdS–In_2S_3 binary composites for producing H_2 and N-BDBA is significantly improved. The amount of H_2 and N-BDBA produced over blank In_2S_3 and x%-PdS–In_2S_3 exhibits a volcano-type curve with the increase of the PdS amount. Particularly, 3%-PdS–In_2S_3 shows the

highest H_2 and N-BDBA yields of 41.62 μmol and 38.46 μmol, which are ca. 39.8- and 14.3-fold higher than that of the blank In_2S_3. Excessive introduction of PdS leads to reduced photoactivity, which is mainly due to the fact that excessive PdS loading may hinder the active site and the light absorption of In_2S_3.[29,44] Furthermore, the molar ratios of the N-BDBA and H_2 during the process were measured to be ca. 1.0, revealing that the dehydrogenation reaction proceeds in chemically stoichiometric conditions.[1] For investigating the connection of photo-absorption with catalytic performance, wavelength correlation experiments were conducted in which the light intensity is the same. As can be seen in Fig. 3c, the photocatalytic activity of the 3%-PdS–In_2S_3 composite decreases with the increase in wavelength, which explicitly

Table 1 Range of application for the oxidation of aromatic amines to imines and H_2 evolution[a]

Entry	Substrate	Liquid product	Conversion[b] (%)	Selectivity[c] (%)	Generation rate[d] (μmol h^{-1}) Liquid product	H$_2$	Carbon balance[e] (%)	R (e^{-}/h^{+})[f]
1			64	>99	16.0	17.0	100.4	1.06
2			58	>99	14.5	14.5	99.5	1.00
3			52	>99	12.9	12.1	100.2	0.93
4			37	>99	9.8	10.5	100	1.06
5			68	>99	16.9	13.2	99.8	0.78
6			72	>99	18.0	16.9	99.8	0.94
7			23	>99	5.6	6.8	100	1.20
8			71	>99	18.6	21.2	99.5	1.14
9			45	>99	11.2	11.7	99.7	1.05
10			41	>99	10.3	9.4	100	0.91
11			31	>99	9.7	7.6	99.3	0.97
12			74	>99	18.5	19.6	100	1.06

[a] Reaction conditions: 5 mg of 3%-PdS–In_2S_3 photocatalysts and 0.1 mmol of reactants were added in 10 mL of acetonitrile (MeCN). The suspension was degassed under Ar for 0.5 h and then illuminated by visible light for 2 h at normal temperature and atmospheric pressure. [b] Conversion (%) = $(n_0 - n)/n_0 \times 100\%$. [c] Selectivity (%) is based on the GC-MS analysis. [d] Generation rate = n_1/t. [e] Carbon balance (%) = $(2n_1 + n_2)/(n_0 - n) \times 100\%$. [f] The electrons-to-holes ratio involved in the redox process was derived by the following equation of e^{-}/h^{+} = $2n(H_2)/(n_0 - n)$, where n_0 and n are the amounts of the initial and the residual amines, respectively, n_1 and n_2 represent the amount of imine and by-products, respectively, and t represents the reaction time (2 h).

demonstrates the dependence on visible light to drive the process.

Stability and recyclability are the essential criteria for evaluating the performance of photocatalysts. The reaction time curves (Fig. 3d and S5†) show that the conversion of benzylamine gradually increases with the extension of the reaction time, and about 95% of benzylamine can be converted within 4 h, which further illustrates the excellent photo-oxidative reduction efficiency of the composites. As demonstrated in Fig. 3e, after 6 cycles in 12 h, the amount of H_2 and N-BDBA generated by the 3%-PdS–In_2S_3 remained basically unchanged, and no obvious inactivation was observed. Based on these positive results, in order to validate the tolerability of our cooperative photoredox-catalyzed system, the substrate range for the amine dehydrocoupling reaction was extended. As can be seen from Table 1, the PdS–In_2S_3 photocatalysts exhibit high selectivity for different substrates, while the variation of substrates affects the yields of the corresponding imines. Specifically, the transformation of primary amines with electron-absorbing groups is

marginally more moderate than that of imines with electron-donating groups (entries 1–8), and the rate of reaction of the regional isomers increases in the order of *ortho* < *meta* < *para*, revealing a steric effect (entries 4–10). The above-mentioned results indicate that both electronic and site-blocking effects significantly affect the reaction.[45] Noticeably, the catalysts also exhibit favorable activity for heteroatom-containing amines (entries 11 and 12). In addition, no other by-products were observed by GC-MS analysis (Fig. S6–S15†). The ratio of electrons to holes ($R(e^-/h^+)$, REH) participating in the photoredox reactions is one of the key indexes defining the catalytic performance, and was calculated to be about 100% in the photo-oxidation reaction described above,[1] implying that the dehydrogenation reaction of the dual-functional photocatalytic system is chemically stoichiometric, thus unveiling the effectiveness of cooperative photoredox-catalyzed amine conversion and H_2 production on PdS–In_2S_3.

In an attempt to examine the causes of the enhanced photocatalytic performance of the 3%-PdS–In_2S_3 binary complex compared to the blank In_2S_3, a series of
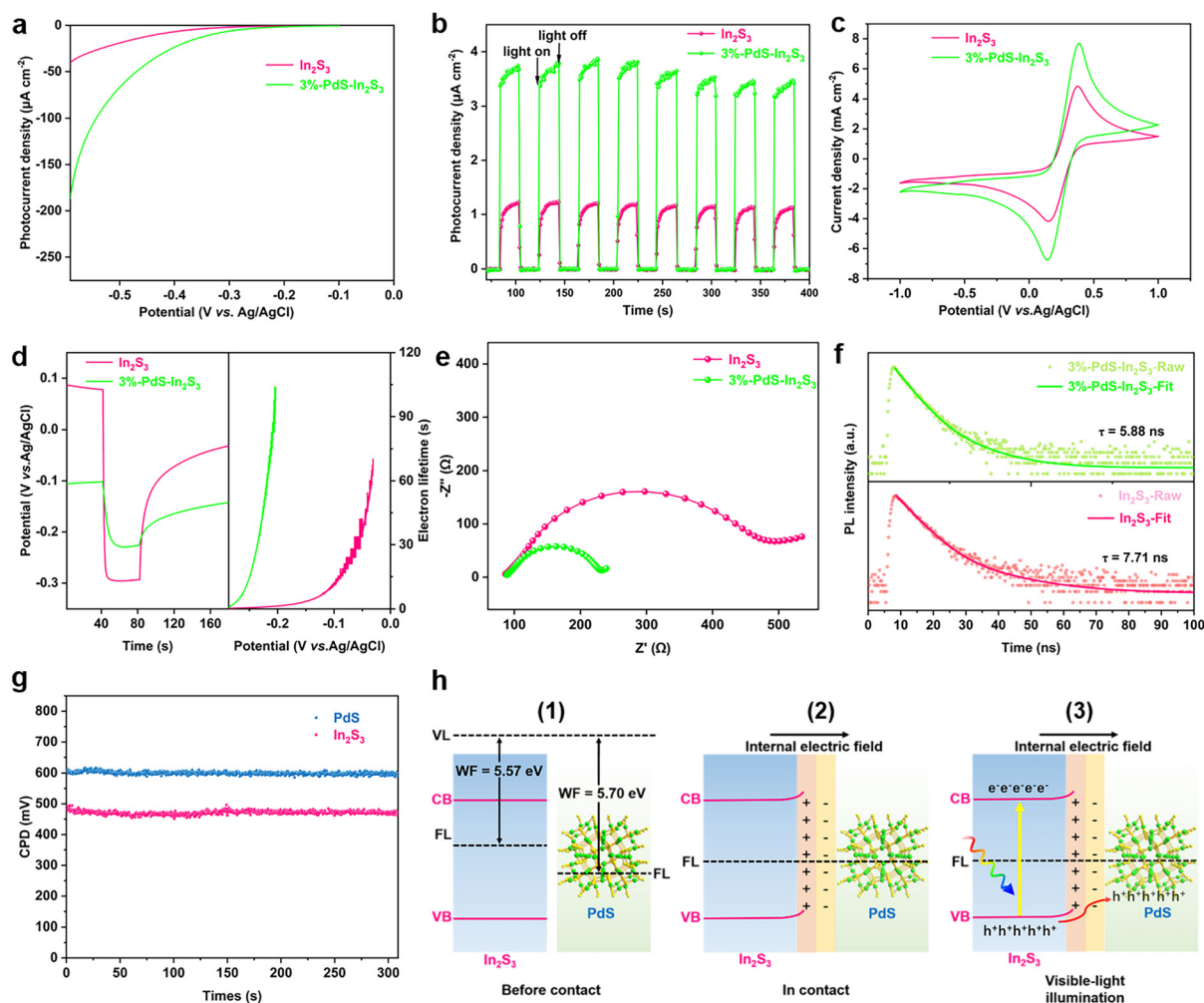
Fig. 4 (a) Polarization curves. (b) Transient photocurrent spectra. (c) CV curves. (d) Decay curves of photovoltage (left) and electron lifetime (right). (e) EIS Nyquist plots. (f) TRPL spectra of In_2S_3 and 3%-PdS–In_2S_3, respectively. (g) CPD of PdS and In_2S_3. (h) The schematic diagrams of the proposed IEF formation and carrier transfer processes (1), (2), and (3).

© 2024 The Author(s). Co-published by the Institute of Process Engineering, Chinese Academy of Sciences and the Royal Society of Chemistry

Ind. Chem. Mater., 2024, **2**, 289–299 | **293**

electrochemical, photoelectron-chemical, and photoluminescence (PL) measurements were taken, which are closely correlated with the reaction kinetics of photogenerated charge carriers.[46] Fig. 4a presents the linear sweep voltammetry (LSV) curves of 3%-PdS–In$_2$S$_3$ and bare In$_2$S$_3$. With the introduction of PdS, the initial overpotential of the binary sample is increased, thus accelerating the reduction of protons to H$_2$.[47] As sketched in Fig. 4b, an enhanced photocurrent response is observed for 3%-PdS–In$_2$S$_3$ compared to that of bare In$_2$S$_3$, implying that the photogenerated charge pair recombination in 3%-PdS–In$_2$S$_3$ samples is effectively improved. The cyclic voltammetry (CV) curves in Fig. 4c also support the above results.[48] The open-circuit photovoltage (OCP) and consequent attenuation analyses demonstrate that bare In$_2$S$_3$ exhibits a shorter electron lifetime than the 3%-PdS–In$_2$S$_3$ (Fig. 4d), which suggests that the separation of photogenerated carriers is faster on 3%-PdS–In$_2$S$_3$.[49] Furthermore, electrochemical impedance spectroscopy (EIS) was employed to probe the charge transfer resistance on the contact interface of the sample and working electrolyte.[50] Fig. 4e exhibits that the curvature radius of the EIS plot of 3%-PdS–In$_2$S$_3$ is smaller than that of the blank In$_2$S$_3$, revealing a lower resistance and faster charge transfer between the 3%-PdS–In$_2$S$_3$ composite and the electrolyte. The mentioned inferences are further supported by PL and time-resolved PL (TRPL) spectra, which are broadly applied to determine the state of photogenerated charge carriers.[51] As shown in Fig. S16,† the PL spectra of both composites show similar emission peak characteristics at approximately 650 nm (λ_{ex} = 360 nm), and a significant diminution of the PL intensity of 3%-PdS–In$_2$S$_3$ is observed by the modification of PdS. Furthermore, by calculating the average charge lifetime (τ_a) and fitting the exponential decay dynamic function (Fig. 4f and Table S2†), the average emission lifetime of In$_2$S$_3$ (7.71 ns) was found to be longer than that of 3%-PdS–In$_2$S$_3$ (5.88 ns), demonstrating that a faster interface charges transfer is achieved in 3%-PdS–In$_2$S$_3$.[34] In a nutshell, the above comparative analysis measurements elucidate that the load of PdS can significantly improve the separation and migration of In$_2$S$_3$ electron–hole pairs, resulting in a noteworthy enhancement of the photocatalytic performance.

For a deep investigation of the interfacial charge transfer route from PdS to In$_2$S$_3$, a Kelvin probe device was utilized to determine the contact potential difference (CPD, mV) of the composites in dark conditions, through which the work function (WF) of the In$_2$S$_3$ and PdS can be obtained. As shown in Fig. 4g, the CPD of In$_2$S$_3$ to the gold probe is 470 mV, and the CPD of PdS to the gold probe is 600 mV. Thus, the WFs of PdS and In$_2$S$_3$ are determined as 5.70 eV and 5.57 eV, respectively, by the relationship of WF (eV) = 5.1 + e × CPD/1000 (where the e represents an electron and the 5.1 eV is the WF of the gold probe).[52] Compared with PdS, the WF of In$_2$S$_3$ is lower, which signifies that electronic escaping in In$_2$S$_3$ is kinetically easier.[52] Therefore, upon intimate contact between In$_2$S$_3$ and PdS, a spontaneous transfer takes place

via the intimate interface of electrons from In$_2$S$_3$ to PdS until the equilibrium is reached at their Fermi level (FL). As the electrons are withdrawn, the energy band of In$_2$S$_3$ bends upwards, which leads to an accumulation of positive charges on In$_2$S$_3$ with the negative charges on PdS, resulting in the formation of the interfacial electric field (IEF) directing from In$_2$S$_3$ to PdS.[53] When illuminated by visible light, the relocation of photoexcited holes remaining on the valence band (VB) of In$_2$S$_3$ to PdS is accelerated by the forceful driving force served by the IEF, while the photogenerated electrons on the conduction band (CB) of In$_2$S$_3$ are blocked back to In$_2$S$_3$ by IEF and the upward energy band bending (Fig. 4h).

In order to better reveal the potential dual photoredox reaction mechanism of the photocatalytic process, a range of control and quenching tests were carried out. As shown in Fig. 5a, no product was detected in the absence of catalyst or light, indicating that the reaction is a light-driven catalytic process. Upon incorporation of the electron scavenger carbon tetrachloride (CCl$_4$), the evolution of H$_2$ stops, which implies that photoexcited electrons play a vital role in H$_2$ evolution. Significantly, the *N*-BDBA product is significantly hindered by the involvement of the hole scavenger triethanolamine (TEOA), whereas the REH value of the reaction is calculated to be *ca.* 1.0, which suggests that the oxidation and reduction reactions of the system are intimately interrelated. Thermodynamic constraints require that the CB and VB potentials of In$_2$S$_3$ should be lower than the reduction potential of H$^+$/H$_2$ (−0.41 V *vs.* NHE) and higher than the oxidation potential of BA/BA$^{·+}$, respectively, in order to make these two half-reactions proceed successfully. By analyzing the Mott–Schottky curve (Fig. S17†), the band gap structure of In$_2$S$_3$ is obtained. The positive slope of the linear plot indicates that In$_2$S$_3$ is an n-type semiconductor. The VB potential of In$_2$S$_3$ of −0.81 V *vs.* Ag/AgCl can be transformed to −0.61 V *vs.* the normal hydrogen electrode (NHE) according to the equation of $E_{NHE} = E_{Ag/AgCl} + 0.20$ V.[20] Thereby, the CB value of In$_2$S$_3$ can be evaluated as −0.61 V, while the VB value of In$_2$S$_3$ is 1.57 V depending on the equation $E_{VB} = E_{CB} + E_g$.[25] Moreover, depending on the CV curve, the oxidation potential of BA is measured to be 0.84 V *vs.* Ag/AgCl (Fig. S18†), which is equal to 1.04 V *vs.* NHE. Therefore, the dual-function photocatalytic system is thermodynamically feasible.

Additionally, *in situ* Fourier transform-infrared spectroscopy (FT-IR) was employed to obtain insights into the dynamic evolutionary characterization of the reaction (Fig. 5b and c). With the progress of the reaction, characteristic peaks appear at 3278 cm^{-1} and 3366 cm^{-1}, belonging to the symmetric and asymmetric stretching vibration of the N–H bond, respectively, and at 2858 cm^{-1} and 2920 cm^{-1}, belonging to the symmetric stretching vibration bands of the methylene bond. The decrease in the intensity of the above characteristic peaks indicates that benzylamine is being consumed.[54] Meanwhile, the intensity of the newly formed peak at 1645 cm^{-1} corresponding to C=N progressively increases with the extension of the
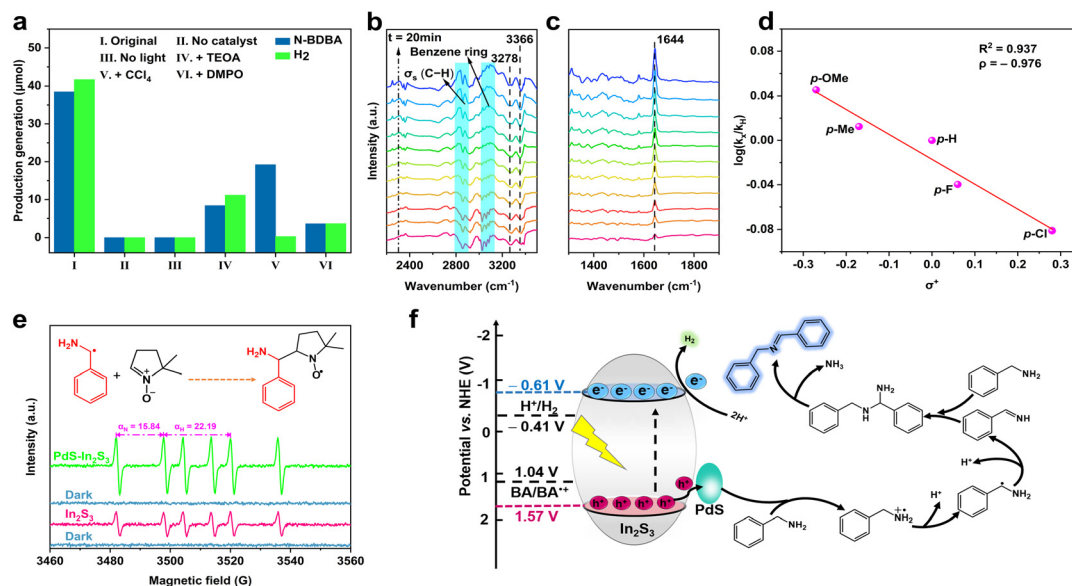
Fig. 5 (a) Control experiments and quenching experiments with varying reagents over 3%-PdS–In$_2$S$_3$. (b) and (c) Time-dependent *in situ* FTIR spectra of 3%-PdS–In$_2$S$_3$. (d) Hammett analysis of electronically disparate BA over 3%-PdS–In$_2$S$_3$. (e) The quantitative analysis result of EPR spectrums of 3%-PdS–In$_2$S$_3$ in Ar-saturated CH$_3$CN solution in the presence of BA and DMPO. (f) Proposed mechanism of H$_2$ evolution and BA transformation by visible photocatalysis on PdS–In$_2$S$_3$.

lighting duration, indicating the formation of *N*-BDBA. In addition, the characteristic peaks at 3025 cm^{-1}, 3061 cm^{-1} and 3084 cm^{-1} belong to the stretching vibration of the C–H bond of the benzene ring, and the increase in the intensity of the peaks can be attributed to the generation of *N*-BDBA.[55]

Clarifying the structure of the reaction intermediates is of major importance, for which further radical-quenching tests and electron paramagnetic resonance (EPR) were performed. When the radical trapping agent of 5,5-dimethyl-1-pyrroline-*N*-oxide (DMPO) is added, the photocatalytic activity of the materials is markedly weakened, which indicates the forming of reactive radical intermediates in the process of the reaction. For identifying the vital intermediate of BA oxidation, the Hammett plot for photocatalytic selective oxidation of various *para*-substituted BA combined with H$_2$ evolution over 3%-PdS–In$_2$S$_3$ was obtained, as shown in Fig. 5d.[56] The outcomes demonstrate that the Brown–Okamoto constants (σ^+) of the side groups (F, Me, MeO, Cl, and H) have a well-reasoned linear correlation with the log(k_X/k_H) values (reaction constant of $\rho = -0.967$), which not only indicates that the cationic species (PhCH$_2$NH$_2^{\bullet+}$) are generated during BA oxidation, but also confirms that the cleavage of α-C–H bonds is the rate-limiting step for the formation of *N*-BDBA.[3,57] Furthermore, to gain further insight into the details of the reactive intermediates in this photocatalytic system, the EPR technique was employed to characterize the radical intermediate in the reaction with DMPO as the scavenger. As portrayed in Fig. 5e, upon light illumination, six characteristic peaks with similar intensity are observed on both 3%-PdS–In$_2$S$_3$ and blank In$_2$S$_3$, which can be ascribed to the DMPO–PhCHNH$_2$ signal, indicating the generation of Ph($\bullet$CH)NH$_2$ free radical (α_N = 16.03 and α_H

= 22.97).[58] In addition, the signal belonging to DMPO–PhCHNH$_2$ on the blank In$_2$S$_3$ is weaker than that of 3%-PdS–In$_2$S$_3$, which is consistent with the above photoactivity trend.

Given the foregoing discussion, an underlying mechanism of dehydrocoupling of BA to *N*-BDBA on 3%-PdS–In$_2$S$_3$ is put forward as follows: as shown in Fig. 5f, upon irradiation by visible light, the In$_2$S$_3$ nanospheres are optically excited to produce the hole–electron pairs. Subsequently, as the IEF is formed by the tight interfacial contact and matched energy level arrangement between In$_2$S$_3$ and PdS in the binary composite the photogenerated holes are trapped expeditiously by PdS, while the photogenerated electrons are blocked back to the CB of In$_2$S$_3$. The holes trapped by PdS first attack BA to form the cationic species of PhCH$_2$NH$_2^{\bullet+}$, which is then converted to Ph($\bullet$CH)NH$_2$ radicals through deprotonation. Subsequently, the generated radicals of Ph($\bullet$CH)NH$_2$ are further attacked by the photogenerated holes to form the imine intermediate of (phenyl)methenamine, then eventually, the (phenyl)methanimine interacts with another BA molecule to form *N*-benzyl-1-phenylmethylenediamine,[59] which readily undergoes an addition–elimination reaction, thus ensuring the elimination of ammonia in the resulting *N*-BDBA (Fig. S19†). Meanwhile, the protons generated in the process are reduced to H$_2$ by photogenerated electrons on the CB of In$_2$S$_3$.

3 Conclusion

In summary, binary PdS–In$_2$S$_3$ composites have been successfully fabricated for the efficient photocatalytic oxidation of amines to imines paired with H$_2$ production under visible light irradiation. The matched energy levels

© 2024 The Author(s). Co-published by the Institute of Process Engineering, Chinese Academy of Sciences and the Royal Society of Chemistry

Ind. Chem. Mater., 2024, **2**, 289–299 | **295**

together with the fabrication of an internal electric field between In_2S_3 and PdS accelerate the separation and migration of photogenerated charge carriers, leading to significantly enhanced photoactivity for amine dehydrogenation coupling. The Ph($\cdot$CH)NH$_2$ radical has been demonstrated to be the vital reactive intermediate in this photoredox-catalyzed process. Furthermore, such a reaction system not only exhibits great compatibility with a variety of amines, but also affords excellent selectivity and stability. This work is anticipated to assist in the judicious construction of photocatalysts with reasonable modification to adequately use photoexcited carriers simultaneously, offering a prospective and economic pathway for the synthesis of high-value-added chemical compounds.

4 Experimental section

4.1 Materials

Sodium sulfide nonahydrate ($Na_2S\cdot9H_2O$), indium chloride tetrahydrate ($InCl_3\cdot4H_2O$), thiosemicarbazide (CH_5N_3S), anhydrous ethanol (C_2H_6O), and acetonitrile (MeCN) were provided by Sinopharm Chemical Reagent Co., Ltd. (Shanghai, China). Benzylamine (C_7H_9N, BA), sodium tetrachloropalladate (Na_2PdCl_4), and Nessler's reagent were obtained from Aladdin Biochemical Technology Co. Ltd. (Shanghai, China). No further processing was done to the reagents and they were all used as presented. Deionized (DI) water was obtained from local sources.

4.2 Synthesis of In_2S_3 nanospheres

The blank In_2S_3 nanospheres were synthesized according to previous reports with some modifications.[60] Detailed preparation procedures are described in the ESI.†

4.3 Synthesis of PdS–In_2S_3 composites

The PdS–In_2S_3 composites were prepared *via in situ* chemical deposition.[61] Typically, a quantity of the as-synthesized In_2S_3 nanospheres was ultrasonically dispersed into 50 mL of 100 mM $Na_2S\cdot9H_2O$ aqueous solution for some minutes, then stirred vigorously at room temperature for a moment. Subsequently, a calculated volume of 10 mM Na_2PdCl_4 aqueous solution was rapidly injected under intense agitation. Then, the suspension was exposed to light and stirred vigorously for 0.5 h. The resultant composites were filtered and washed with absolute ethanol and finally dried overnight in a vacuum oven. The obtained catalysts with different mass ratios were named x%-PdS–In_2S_3 (x = 0.2, 0.5, 1, 3, 5, and 7), where the x represents the coefficient of the theoretical mass ratio of PdS to In_2S_3.

4.4 Photocatalytic performance testing

The photoactivity testing was carried out based on previous research with some adaptations. In a typical process, 5 mg of photocatalyst, 10 mL of MeCN, and 0.1 mmol of BA were placed into a double-layer quartz reactor. Prior to illumination, argon (Ar) gas was used to purge the reactor for 0.5 h to completely remove air. Then, the suspension was exposed under visible light (λ > 420 nm) by a 300 W Xe lamp (CEL-HXF300-T3, Beijing China Education Au-light Co., Ltd., China). Finally, the reactor was connected to circulating condensate for the reaction. A gas chromatograph (Shimadzu GC-8A 2014C, MS-5A column) was employed to quantify the generated H_2. Liquid products were detected through GC-MS (Shimadzu GC-MS QP 2020, Q-Exactive).

Author contributions

Yu Chen: investigation, confirmation, writing-original draft, data analysis, and writing-review & editing. Chang-Long Tan: formal analysis and writing-review & editing. Jing-Yu Li: writing-review & editing. Ming-Yu Qi: writing-review & editing. Zi-Rong Tang: funding acquisition, formal analysis, conceptualization, resources, and supervision. Yi-Jun Xu: funding acquisition, conceptualization, resources, project administration, and supervision.

Conflicts of interest

The authors declare no conflicting interests.

References

1 M.-Y. Qi, M. Conte, M. Anpo, Z.-R. Tang and Y.-J. Xu, Cooperative coupling of oxidative organic synthesis and hydrogen production over semiconductor-based photocatalysts, *Chem. Rev.*, 2021, **121**, 13051–13085.
2 N. Li, X. Lang, W. Ma, H. Ji, C. Chen and J. Zhao, Selective aerobic oxidation of amines to imines by TiO_2 photocatalysis in water, *Chem. Commun.*, 2013, **49**, 5034–5036.
3 H. Liu, C. Xu, D. Li and H. L. Jiang, Photocatalytic hydrogen production coupled with selective benzylamine oxidation over MOF composites, *Angew. Chem., Int. Ed.*, 2018, **57**, 5379–5383.
4 H. Chen, C. Liu, M. Wang, C. Zhang, N. Luo, Y. Wang, H. Abroshan, G. Li and F. Wang, Visible light gold nanocluster photocatalyst: Selective aerobic oxidation of amines to imines, *ACS Catal.*, 2017, **7**, 3632–3638.
5 B. Chen, L. Wang and S. Gao, Recent advances in aerobic oxidation of alcohols and amines to imines, *ACS Catal.*, 2015, **5**, 5851–5876.

296 | *Ind. Chem. Mater.*, 2024, **2**, 289–299

© 2024 The Author(s). Co-published by the Institute of Process Engineering, Chinese Academy of Sciences and the Royal Society of Chemistry

6 C. Han, Y.-H. Li, J.-Y. Li, M.-Y. Qi, Z.-R. Tang and Y.-J. Xu, Cooperative syngas production and C–N bond formation in one photoredox cycle, *Angew. Chem., Int. Ed.*, 2021, **60**, 7962–7970.

7 Y. Ren, J. Zou, K. Jing, Y. Liu, B. Guo, Y. Song, Y. Yu and L. Wu, Photocatalytic synthesis of N-benzyleneamine from benzylamine on ultrathin BiOCl nanosheets under visible light, *J. Catal.*, 2019, **380**, 123–131.

8 P. Wang, X. Li, S. Fan, Z. Yin, L. Wang, M. O. Tadé and S. Liu, Piezotronic effect and oxygen vacancies boosted photocatalysis C–N coupling of benzylamine, *Nano Energy*, 2021, **83**, 105831.

9 Z. J. Wang, S. Ghasimi, K. Landfester and K. A. Zhang, Molecular structural design of conjugated microporous poly(benzooxadiazole) networks for enhanced photocatalytic activity with visible light, *Adv. Mater.*, 2015, **27**, 6265–6270.

10 K. X. Zhang, H. Su, H. H. Wang, J. J. Zhang, S. Y. Zhao, W. Lei, X. Wei, X. H. Li and J. S. Chen, Atomic-scale Mott-Schottky heterojunctions of boron nitride monolayer and graphene as metal-free photocatalysts for artificial photosynthesis, *Adv. Sci.*, 2018, **5**, 1800062.

11 S. Wei, H. Zhong, H. Wang, Y. Song, C. Jia, M. Anpo and L. Wu, Oxygen vacancy enhanced visible light photocatalytic selective oxidation of benzylamine over ultrathin Pd/BiOCl nanosheets, *Appl. Catal., B*, 2022, **305**, 121032.

12 P. Wang, S. Fan, X. Li, J. Wang, Z. Liu, C. Bai, M. O. Tadé and S. Liu, Piezotronic effect and hierarchical Z-scheme heterostructure stimulated photocatalytic H_2 evolution integrated with C-N coupling of benzylamine, *Nano Energy*, 2021, **89**, 106349.

13 V. Soni, P. Raizada, A. Kumar, V. Hasija, S. Singal, P. Singh, A. Hosseini-Bandegharaei, V. K. Thakur and V.-H. Nguyen, Indium sulfide-based photocatalysts for hydrogen production and water cleaning: A review, *Environ. Chem. Lett.*, 2021, **19**, 1065–1095.

14 J. Zhang, H. Wang, X. Yuan, G. Zeng, W. Tu and S. Wang, Tailored indium sulfide-based materials for solar-energy conversion and utilization, *J. Photochem. Photobiol., C*, 2019, **38**, 1–26.

15 F. Zhang, X. Li, Q. Zhao and A. Chen, Facile and controllable modification of 3D In_2O_3 microflowers with In_2S_3 nanoflakes for efficient photocatalytic degradation of gaseous ortho-dichlorobenzene, *J. Phys. Chem. C*, 2016, **120**, 19113–19123.

16 X. Sun, X. Luo, X. Zhang, J. Xie, S. Jin, H. Wang, X. Zheng, X. Wu and Y. Xie, Enhanced superoxide generation on defective surfaces for selective photooxidation, *J. Am. Chem. Soc.*, 2019, **141**, 3797–3801.

17 W. Tian, C. Chen, L. Meng, W. Xu, F. Cao and L. Li, PVP treatment induced gradient oxygen doping in In_2S_3 nanosheet to boost solar water oxidation of WO_3 nanoarray photoanode, *Adv. Energy Mater.*, 2020, **10**, 1903951.

18 M.-Q. Yang, B. Weng and Y.-J. Xu, Improving the visible light photoactivity of In_2S_3-graphene nanocomposite via a simple surface charge modification approach, *Langmuir*, 2013, **29**, 10549–10558.

19 X. Fu, X. Wang, Z. Chen, Z. Zhang, Z. Li, D. Y. C. Leung, L. Wu and X. Fu, Photocatalytic performance of tetragonal and cubic β-In_2S_3 for the water splitting under visible light irradiation, *Appl. Catal., B*, 2010, **95**, 393–399.

20 Y. Liu, C. Chen, Y. He, Z. Zhang, M. Li, C. Li, X. B. Chen, Y. Han and Z. Shi, Rich indium-vacancies In_2S_3 with atomic p-n homojunction for boosting photocatalytic multifunctional properties, *Small*, 2022, **18**, e2201556.

21 T. Yan, J. Tian, W. Guan, Z. Qiao, W. Li, J. You and B. Huang, Ultra-low loading of Ag_3PO_4 on hierarchical In_2S_3 microspheres to improve the photocatalytic performance: The cocatalytic effect of Ag and Ag_3PO_4, *Appl. Catal., B*, 2017, **202**, 84–94.

22 X. Han, B. Lu, X. Huang, C. Liu, S. Chen, J. Chen, Z. Zeng, S. Deng and J. Wang, Novel p- and n-type S-scheme heterojunction photocatalyst for boosted CO_2 photoreduction activity, *Appl. Catal., B*, 2022, **316**, 121587.

23 Q. Kang, X. Yin, R. Liu, S. Meng, X. Xu, B. Su, Z. Yang and Z. Lei, Hollow multi-shelled In_2S_3 hierarchical nanotubes for enhanced photocatalytic oxidative coupling of benzylamine, *J. Solid State Chem.*, 2022, **310**, 123087.

24 J.-H. Zheng, M.-Y. Qi, Z.-R. Tang and Y.-J. Xu, Manipulating selective amine transformation pathways via cocatalyst-modified monolayer $ZnIn_2S_4$ photocatalysts, *J. Mater. Chem. A*, 2023, **11**, 4013–4019.

25 X. Ma, W. Li, H. Li, M. Dong, X. Li, L. Geng, H. Fan, Y. Li, H. Qiu and T. Wang, Fabrication of novel and noble-metal-free MoP/In_2S_3 Schottky heterojunction photocatalyst with efficient charge separation for enhanced photocatalytic H_2 evolution under visible light, *J. Colloid Interface Sci.*, 2022, **617**, 284–292.

26 Y. Zhu, G. Xie, G. Li, F. Song, C. Yu, Z. Wu, X. Xie and N. Zhang, Facial synthesis of two-dimensional $In_2S_3/Ti_3C_2T_x$ heterostructures with boosted photoactivity for the hydrogenation of nitroaromatic compounds, *Mater. Chem. Front.*, 2021, **5**, 6883–6890.

27 X. Li, X. Lyu, X. Zhao, Y. Zhang, S. N. Akanyange, J. C. Crittenden, H. Zhao and T. Jiang, Enhanced photocatalytic H_2 evolution over In_2S_3 via decoration with GO and Fe_2P co-catalysts, *Int. J. Hydrogen Energy*, 2021, **46**, 18376–18390.

28 M. Wang, G. Zhang, Z. Guan, J. Yang and Q. Li, Spatially separating redox centers and photothermal effect synergistically boosting the photocatalytic hydrogen evolution of $ZnIn_2S_4$ nanosheets, *Small*, 2021, **17**, e2006952.

29 R. Zhang, X. Jia, Y. Li, X. Yu and Y. Xing, Oxidation co-catalyst modified In_2S_3 with efficient interfacial charge transfer for boosting photocatalytic H_2 evolution, *Int. J. Hydrogen Energy*, 2022, **47**, 25300–25308.

30 F. Zhao, N. Zhang, H. Li, X. Zhang, Z. Luo and Y. Wang, Photocatalyst with chloroplast-like structure for enhancing hydrogen evolution reaction, *Energy Environ. Mater.*, 2021, **5**, 1229–1237.

31 Q. Sun, N. Wang, J. Yu and J. C. Yu, A hollow porous CdS photocatalyst, *Adv. Mater.*, 2018, **30**, e1804368.

32 K. Khan, X. Tao, M. Shi, B. Zeng, Z. Feng, C. Li and R. Li, Visible-light-driven photocatalytic hydrogen production on

© 2024 The Author(s). Co-published by the Institute of Process Engineering, Chinese Academy of Sciences and the Royal Society of Chemistry

Ind. Chem. Mater., 2024, **2**, 289–299 | **297**

$Cd_{0.5}Zn_{0.5}S$ nanorods with an apparent quantum efficiency exceeding 80%, *Adv. Funct. Mater.*, 2020, **30**, 2003731.

33 B. Qiu, M. Du, Y. Ma, Q. Zhu, M. Xing and J. Zhang, Integration of redox cocatalysts for artificial photosynthesis, *Energy Environ. Sci.*, 2021, **14**, 5260–5288.

34 C.-L. Tan, M.-Y. Qi, Z.-R. Tang and Y.-J. Xu, Cocatalyst decorated $ZnIn_2S_4$ composites for cooperative alcohol conversion and H_2 evolution, *Appl. Catal., B*, 2021, **298**, 120541.

35 C. Feng, Z. P. Wu, K. W. Huang, J. Ye and H. Zhang, Surface modification of 2D photocatalysts for solar energy conversion, *Adv. Mater.*, 2022, **34**, e2200180.

36 B. Sun, J. Zheng, D. Yin, H. Jin, X. Wang, Q. Xu, A. Liu and S. Wang, Dual cocatalyst modified CdS achieving enhanced photocatalytic H_2 generation and benzylamine oxidation performance, *Appl. Surf. Sci.*, 2022, **592**, 153277.

37 G. Sun, S. Mao, D. Ma, Y. Zou, Y. Lv, Z. Li, C. He, Y. Cheng and J.-W. Shi, One-step vulcanization of Cd(OH)Cl nanorods to synthesize CdS/ZnS/PdS nanotubes for highly efficient photocatalytic hydrogen evolution, *J. Mater. Chem. A*, 2019, **7**, 15278–15287.

38 X.-l. Li, G.-Q. Yang, S.-S. Li, N. Xiao, N. Li, Y.-Q. Gao, D. Lv and L. Ge, Novel dual co-catalysts decorated Au@HCS@PdS hybrids with spatially separated charge carriers and enhanced photocatalytic hydrogen evolution activity, *Chem. Eng. J.*, 2020, **379**, 122350.

39 Z. Zhang, D. Jiang, D. Li, M. He and M. Chen, Construction of $SnNb_2O_6$ nanosheet/g-C_3N_4 nanosheet two-dimensional heterostructures with improved photocatalytic activity: Synergistic effect and mechanism insight, *Appl. Catal., B*, 2016, **183**, 113–123.

40 S. Zhang, H. Yang, H. Gao, R. Cao, J. Huang and X. Xu, One-pot synthesis of CdS irregular nanospheres hybridized with oxygen-incorporated defect-rich MoS_2 ultrathin nanosheets for efficient photocatalytic hydrogen evolution, *ACS Appl. Mater. Interfaces*, 2017, **9**, 23635–23646.

41 X. Ma, K. Zhao, H. Tang, Y. Chen, C. Lu, W. Liu, Y. Gao, H. Zhao and Z. Tang, New insight into the role of gold nanoparticles in Au@CdS core-shell nanostructures for hydrogen evolution, *Small*, 2014, **10**, 4664–4670.

42 N. Zhang, S.-Q. Liu, X.-Z. Fu and Y.-J. Xu, Synthesis of M@TiO_2 (M = Au, Pd, Pt) core-shell nanocomposites with tunable photoreactivity, *J. Phys. Chem. C*, 2011, **115**, 9136–9145.

43 J.-Y. Li, Y.-H. Li, N. Zhang, Z.-R. Tang and Y.-J. Xu, Visible-light-driven integrated organic synthesis and hydrogen evolution over 1D/2D CdS-Ti_3C_2Tx MXene composites, *Appl. Catal., B*, 2020, **269**, 118783.

44 Q. Lin, Y.-H. Li, M.-Y. Qi, J.-Y. Li, Z.-R. Tang, M. Anpo, Y. M. A. Yamada and Y.-J. Xu, Photoredox dual reaction for selective alcohol oxidation and hydrogen evolution over nickel surface-modified $ZnIn_2S_4$, *Appl. Catal., B*, 2020, **271**, 118946.

45 M.-Y. Qi, M. Conte, Z.-R. Tang and Y.-J. Xu, Engineering semiconductor quantum dots for selectivity switch on high-performance heterogeneous coupling photosynthesis, *ACS Nano*, 2022, **16**, 17444–17453.

46 X. Chen, X. Zhang, Y.-H. Li, M.-Y. Qi, J.-Y. Li, Z.-R. Tang, Z. Zhou and Y.-J. Xu, Transition metal doping BiOBr nanosheets with oxygen vacancy and exposed {102} facets for visible light nitrogen fixation, *Appl. Catal., B*, 2021, **281**, 119516.

47 Y.-H. Li, M.-Y. Qi, J.-Y. Li, Z.-R. Tang and Y.-J. Xu, Noble metal free CdS@CuS-Ni_xP hybrid with modulated charge transfer for enhanced photocatalytic performance, *Appl. Catal., B*, 2019, **257**, 117934.

48 S.-H. Li, M.-Y. Qi, Y.-Y. Fan, Y. Yang, M. Anpo, Y. M. A. Yamada, Z.-R. Tang and Y.-J. Xu, Modulating photon harvesting through dynamic non-covalent interactions for enhanced photochemical CO_2 reduction, *Appl. Catal., B*, 2021, **292**, 120157.

49 M.-Y. Qi, Y.-H. Li, F. Zhang, Z.-R. Tang, Y.-j. Xiong and Y.-J. Xu, Switching light for site-directed spatial loading of cocatalysts onto heterojunction photocatalysts with boosted redox catalysis, *ACS Catal.*, 2020, **10**, 3194–3202.

50 C.-L. Tan, M.-Y. Qi, Z.-R. Tang and Y.-J. Xu, Isolated single-atom cobalt in the $ZnIn_2S_4$ monolayer with exposed Zn sites for CO_2 photofixation, *ACS Catal.*, 2023, **13**, 8317–8329.

51 Y.-F. Wang, M.-Y. Qi, M. Conte, Z.-R. Tang and Y.-J. Xu, New radical route and insight for the highly efficient synthesis of benzimidazoles integrated with hydrogen evolution, *Angew. Chem., Int. Ed.*, 2023, **62**, e202304306.

52 J.-Y. Li, C.-L. Tan, M.-Y. Qi, Z.-R. Tang and Y.-J. Xu, Exposed zinc sites on hybrid $ZnIn_2S_4$@CdS nanocages for efficient regioselective photocatalytic epoxide alcoholysis, *Angew. Chem., Int. Ed.*, 2023, **62**, e202303054.

53 W. Li, Z. Wei, Y. Sheng, J. Xu, Y. Ren, J. Jing, J. Yang, J. Li and Y. Zhu, Dual cocatalysts synergistically promote perylene diimide polymer charge transfer for enhanced photocatalytic water oxidation, *ACS Energy Lett.*, 2023, **8**, 2652–2660.

54 H. Chen, C. Liu, W. Guo, Z. Wang, Y. Shi, Y. Yu and L. Wu, Functionalized UiO-66(Ce) for photocatalytic organic transformation: the role of active sites modulated by ligand functionalization, *Catal. Sci. Technol.*, 2022, **12**, 1812–1823.

55 R. H. Alzard, L. A. Siddig, A. S. Abdelhamid and A. Alzamly, Visible-light-driven photocatalytic coupling of neat benzylamine over a Bi-ellagate metal-organic framework, *ACS Omega*, 2022, **7**, 36689–36696.

56 F. Su, S. C. Mathew, L. Mohlmann, M. Antonietti, X. Wang and S. Blechert, Aerobic oxidative coupling of amines by carbon nitride photocatalysis with visible light, *Angew. Chem., Int. Ed.*, 2011, **50**, 657–660.

57 C. Xu, H. Liu, D. Li, J. H. Su and H. L. Jiang, Direct evidence of charge separation in a metal-organic framework: Efficient and selective photocatalytic oxidative coupling of amines via charge and energy transfer, *Chem. Sci.*, 2018, **9**, 3152–3158.

58 J.-Y. Li, M.-Y. Qi and Y.-J. Xu, Efficient splitting of alcohols into hydrogen and C–C coupled products over ultrathin Ni-

doped ZnIn$_2$S$_4$ nanosheet photocatalyst, *Chin. J. Catal.*, 2022, **43**, 1084–1091.

59 X. Liu, D. Dai, Z. Cui, Q. Zhang, X. Gong, Z. Wang, Y. Liu, Z. Zheng, H. Cheng, Y. Dai, B. Huang and P. Wang, Optimizing the reaction pathway by active site regulation in the CdS/Fe$_2$O$_3$ Z-scheme heterojunction system for highly selective photocatalytic benzylamine oxidation integrated with H$_2$ production, *ACS Catal.*, 2022, **12**, 12386–12397.

60 S. Rengaraj, S. Venkataraj, C. W. Tai, Y. Kim, E. Repo and M. Sillanpaa, Self-assembled mesoporous hierarchical-like In$_2$S$_3$ hollow microspheres composed of nanofibers and nanosheets and their photocatalytic activity, *Langmuir*, 2011, **27**, 5534–5541.

61 H. Yan, J. Yang, G. Ma, G. Wu, X. Zong, Z. Lei, J. Shi and C. Li, Visible-light-driven hydrogen production with extremely high quantum efficiency on Pt–PdS/CdS photocatalyst, *J. Catal.*, 2009, **266**, 165–168.

© 2024 The Author(s). Co-published by the Institute of Process Engineering, Chinese Academy of Sciences and the Royal Society of Chemistry

Ind. Chem. Mater., 2024, **2**, 289–299 | **299**